This is a repository copy of *A moving pseudo-boundary method of fundamental solutions for void detection*.

White Rose Research Online URL for this paper:
http://eprints.whiterose.ac.uk/81066/

Version: Accepted Version

# A MOVING PSEUDO-BOUNDARY MFS FOR VOID DETECTION

A. KARAGEORGHIS, D. LESNIC, AND L. MARIN

ABSTRACT. We propose a new moving pseudo-boundary method of fundamental solutions (MFS) for the determination of the boundary of a void. This problem can be modelled as an inverse boundary value problem for harmonic functions. The algorithm for imaging the interior of the medium also makes use of radial polar parametrization of the unknown void shape in two dimensions. The centre of this radial polar parametrization is considered to be unknown. We also include the contraction and dilation factors to be part of the unknowns in the resulting nonlinear least-squares problem. This approach addresses the major problem of locating the pseudo-boundary in the MFS in a natural way since the inverse problem in question is nonlinear anyway. The feasibility of this new method is illustrated by several numerical examples.

## 1. INTRODUCTION

Although the basic ideas behind the MFS had been around long before [1, 22, 23, 24], the MFS was first introduced as a numerical technique in the late seventies in a paper by Mathon and Johnston [27]. In this and the subsequent early papers on the MFS [5, 11, 14, 13, 15] the so called *dynamic* MFS was used. In this approach, the locations of the singularities in the MFS approximation are considered to be part of the unknowns along with the coefficients of the fundamental solutions in the approximation. The unknowns are then determined by collocating the boundary conditions. Because the coordinates of the singularities appear non-linearly, this approach leads to a non-linear least squares minimization problem. The obvious criticism of this approach is that in the case of linear boundary value problems one is required to solve a non-linear discrete problem at a high cost. On the other hand, the *dynamic* approach essentially deals with the long-standing issue of the optimal location of the singularities in the MFS. Although the dynamic approach was applied successfully to non-linear problems [16, 17, 18, 19, 29], it became less popular than the *static* approach in which the singularities are pre-assigned and fixed leading to a linear problem.

In this study we propose the use of a version of the *dynamic* approach for the solution of inverse problems. The MFS has been used extensively in recent years for the solution of various types of inverse problems [21] because of the ease with which it can be implemented. We consider a particular type of inverse problems, the so-called *inverse geometric problems*. These problems are non-linear and the *static* MFS discretization leads to systems of non-linear equations. These are solved using appropriate non-linear least squares minimization software. In view of this nonlinearity, we consider the use of the MFS in which a parameter(s) describing the position(s) of the pseudo-boundary(ies) is(are) taken to be unknowns in the non-linear minimization process at little additional cost. In addition, we consider voids described parametrically by polar coordinates with no knowledge of the centre of this polar system. The coordinates of the centre are taken as additional unknowns in the non-linear minimization process.

The paper is organized as follows. In Section 2 we present the mathematical formulation of the problem. The MFS approximation for this problem is described in Section 3, while the implementational details are given in Section 4. Several numerical examples are investigated in Section 5 and an extension to multiple voids is presented in Section 6. Finally, some comments and conclusions are given in Section 7.

## 2. MATHEMATICAL FORMULATION

In this section we formulate the direct and inverse problems related to a void such as a rigid inclusion or a cavity. The direct mixed problem given by the Laplace equation

$$\Delta u = 0 \quad \text{in} \quad \Omega, \tag{2.1a}$$

subject to the Dirichlet boundary condition

$$u = f \quad \text{on} \quad \partial\Omega_2, \tag{2.1b}$$

and the homogeneous boundary condition

$$\alpha u + (1 - \alpha)\partial_n u = 0 \quad \text{on} \quad \partial\Omega_1, \quad \text{where} \quad \alpha \in \{0, 1\}, \tag{2.1c}$$

has a unique weak solution $u \in \mathcal{H}^1(\Omega)$ if $f \in \mathcal{H}^{1/2}(\partial\Omega_2)$, and a unique classical solution $u \in \mathcal{C}^2(\Omega) \cap \mathcal{C}(\bar\Omega)$, provided $f$ is sufficiently smooth. In the above, $\Omega = \Omega_2 \backslash \Omega_1$, where $\overline\Omega_1 \subset \Omega_2$, is a bounded annular domain with boundary $\partial\Omega = \partial\Omega_1 \cup \partial\Omega_2$. The void $\Omega_1$ may have many connected components, but $\Omega$ should be connected. Equation (2.1c), covers both Dirichlet ($\alpha = 1$), i.e. a rigid inclusion, and Neumann ($\alpha = 0$), i.e. a cavity, boundary conditions on $\partial\Omega_1$.

The inverse problem we are concerned with consists of determining not only the function $u$, but also the void $\Omega_1$ so that $u$ satisfies the Laplace equation (2.1a), given the Dirichlet data $f \not\equiv$ constant in (2.1b), the homogeneous boundary condition (2.1c) and the Neumann current flux measurement

$$g := \partial_n u \quad \text{on} \quad \partial\Omega_2. \tag{2.1d}$$

In (2.1c) and (2.1d), the vector $\boldsymbol{n}$ denotes the outward unit normal to the annular domain $\Omega$.
Clearly, the fact that in the inverse problem the location of $\Omega_1$ is not known is compensated by the additional boundary condition (2.1d). When $\alpha = 0$, for (2.1a), (2.1c) and (2.1d) to be consistent, we require

$$\int_{\partial\Omega_2} g(s)\, ds = 0. \tag{2.2}$$

In contrast to the direct (forward) boundary value problem (2.1a)-(2.1c), the inverse problem (2.1a)-(2.1d) is nonlinear and ill-posed. Although the solution is unique, see [8], it is unstable with respect to small errors in the input Cauchy data (2.1b) and (2.1d). Finally, it is worth mentioning that the uniqueness of identifying multiple voids, e.g. cavities or rigid inclusions, from a single Cauchy data measurement also holds, see [2, 30].

## 3. THE METHOD OF FUNDAMENTAL SOLUTIONS (MFS)

In the application of the MFS to (2.1), we seek an approximation to the solution of Laplace's equation (2.1a) as a linear combination of fundamental solutions of the form [20]

$$u_N(\boldsymbol{c}, \boldsymbol{\xi}; \boldsymbol{x}) = \sum_{k=1}^{2N} c_k\, G(\boldsymbol{\xi}_k, \boldsymbol{x}), \quad \boldsymbol{x} \in \overline\Omega, \tag{3.1}$$

where $G$ is the fundamental solution of the two-dimensional Laplace equation, given by

$$G(\boldsymbol{\xi}, \boldsymbol{x}) = -\frac{1}{2\pi} \ln | \boldsymbol{\xi} - \boldsymbol{x} |. \tag{3.2}$$

The sources $(\boldsymbol{\xi}_k)_{k=\overline{1,2N}}$ are located outside the solution domain $\Omega$, i.e. in $\Omega_1 \cup (\mathbb{R}^2 \backslash \overline\Omega_2)$. In particular, $(\boldsymbol{\xi}_k)_{k=\overline{1,N}} \in \Omega_1$ are placed on a (moving) pseudo-boundary $\partial\Omega_1'$ similar (contraction) to $\partial\Omega_1$, while $(\boldsymbol{\xi}_k)_{k=\overline{N+1,2N}} \in \mathbb{R}^2 \backslash \overline\Omega_2$ are also placed on a (moving) pseudo-boundary $\partial\Omega_2'$ similar (dilation) to $\partial\Omega_2$, as depicted in Figure 1. In the MFS, taking the pseudo-boundary similar to the boundary yields, in general, improved results as has been demonstrated by Gorzelańczyk and Kołodziej [7]. In (3.1), the singularities $(\boldsymbol{\xi}_k)_{k=\overline{N+1,2N}}$ are *not* preassigned. Also, the sources $(\boldsymbol{\xi}_k)_{k=\overline{1,N}}$ move with $\partial\Omega_1$, as will be described in the iterative process presented in the sequel. The fact that the

locations of the pseudo-boundaries $\partial\Omega_1'$ and $\partial\Omega_2'$ are determined as part of the solution takes care of the inherent problem of optimally locating the sources in the MFS.
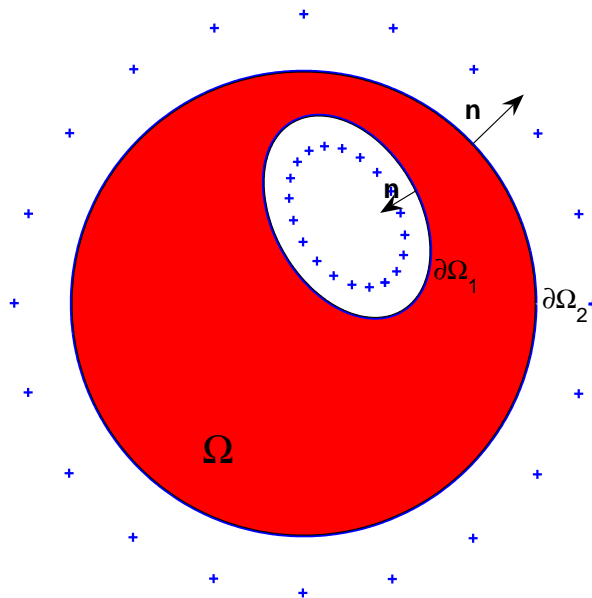


FIGURE 1. Geometry of the problem. The crosses $(+)$ denote the source points.

Without loss of generality, we shall assume that the (known) fixed exterior boundary $\partial\Omega_2$ is a circle of radius $R$. As a result, the outer boundary collocation and source points are chosen as

$$\boldsymbol{x}_{N+\ell} = R(\cos\tilde{\vartheta}_\ell, \sin\tilde{\vartheta}_\ell), \quad \ell = \overline{1,M}, \tag{3.3}$$

$$\boldsymbol{\xi}_{N+k} = \eta_{ext}R(\cos\vartheta_k, \sin\vartheta_k), \quad k = \overline{1,N}, \tag{3.4}$$

respectively, where $\tilde{\vartheta}_\ell = \frac{2\pi(\ell-1)}{M}$, $\ell = \overline{1,M}$ and $\vartheta_k = \frac{2\pi(k-1)}{N}$, $k = \overline{1,N}$, and the (unknown) parameter $\eta_{ext} \in (1,S)$ with $S > 1$ prescribed.

We further assume that the unknown boundary $\partial\Omega_1$ is a smooth, star-like curve with respect to the centre which has unknown coordinates $(X,Y)$. This means that its equation in polar coordinates can be written as

$$x = X + r(\vartheta)\cos\vartheta, \qquad y = Y + r(\vartheta)\sin\vartheta, \qquad \vartheta \in [0,2\pi), \tag{3.5}$$

where $r$ is a smooth $2\pi-$periodic function.

The discretized form of (3.5) for $\partial\Omega_1$ becomes

$$r_k = r(\vartheta_k), \quad k = \overline{1,N} \tag{3.6}$$

and we choose the inner boundary collocation and source points as

$$\boldsymbol{x}_k = (X,Y) + r_k(\cos\vartheta_k, \sin\vartheta_k), \tag{3.7}$$

$$\boldsymbol{\xi}_k = (X,Y) + \eta_{int}r_k(\cos\vartheta_k, \sin\vartheta_k), \quad k = \overline{1,N}, \tag{3.8}$$

where the (unknown) parameter $\eta_{int} \in (0,1)$.

## 4. IMPLEMENTATIONAL DETAILS

The coefficients $(c_k)_{k=\overline{1,2N}}$ in (3.1), the radii $(r_k)_{k=\overline{1,N}} \in (0,1)$ in (3.6), the contraction and dilation coefficients $\eta_{int}$ and $\eta_{ext}$ in (3.8) and (3.4), and the coordinates of the centre $(X, Y)$ can be determined by imposing the boundary conditions (2.1b), (2.1c) and (2.1d) in a least-squares sense. This leads to the minimization of the functional

$$
\begin{aligned}
S(\boldsymbol{c}, \boldsymbol{r}, \boldsymbol{\eta}, \boldsymbol{C}) : \quad = \quad & \sum_{j=N+1}^{N+M} [u_N(\boldsymbol{c}, \boldsymbol{\xi}; \boldsymbol{x}_j) - f^\varepsilon(\boldsymbol{x}_j)]^2 + \sum_{j=N+1}^{N+M} [\partial_n u_N(\boldsymbol{c}, \boldsymbol{\xi}; \boldsymbol{x}_j) - g^\varepsilon(\boldsymbol{x}_j)]^2 \\
& + \sum_{j=1}^{N} [\alpha u_N(\boldsymbol{c}, \boldsymbol{\xi}; \boldsymbol{x}_j) + (1-\alpha)\partial_n u_N(\boldsymbol{c}, \boldsymbol{\xi}; \boldsymbol{x}_j)]^2 + \lambda_1 |\boldsymbol{c}|^2 + \lambda_2 \sum_{\ell=2}^{N} (r_\ell - r_{\ell-1})^2, \quad (4.1)
\end{aligned}
$$

where $\lambda_1, \lambda_2 \geq 0$ are regularization parameters to be prescribed, $\boldsymbol{c} = [c_1, c_2, \ldots, c_{2N}]^T$, $\boldsymbol{r} = [r_1, r_2, \ldots, r_N]^T$, $\boldsymbol{\eta} = [\eta_{int}, \eta_{ext}]^T$ and $\boldsymbol{C} = [X, Y]^T$.

**Note.** It is noteworthy that the current technique of taking $\boldsymbol{\eta}$ as unknown may be used in the solution of the corresponding direct problem in an annular domain where one now needs to minimize the functional

$$
T(\boldsymbol{c}, \boldsymbol{\eta}) := \sum_{j=N+1}^{N+M} [u_N(\boldsymbol{c}, \boldsymbol{\xi}; \boldsymbol{x}_j) - f(\boldsymbol{x}_j)]^2 + \sum_{j=1}^{N} [\alpha u_N(\boldsymbol{c}, \boldsymbol{\xi}; \boldsymbol{x}_j) + (1-\alpha)\partial_n u_N(\boldsymbol{c}, \boldsymbol{\xi}; \boldsymbol{x}_j)]^2. \quad (4.2)
$$

Clearly, in this case, the disadvantage is that one transforms a linear problem into a nonlinear one. However, one does obtain the optimal locations of the inner and outer pseudo-boundaries.

**Remarks.**

(i) The first three terms in equation (4.1) represent a discretized version of the variational form

$$
\|u_N - f^\varepsilon\|^2_{\mathcal{H}^{1/2}(\partial\Omega_2)} + \|\partial_n u_N - g^\varepsilon\|^2_{\mathcal{H}^{-1/2}(\partial\Omega_2)} + \|\alpha u_N + (1-\alpha)\partial_n u_N\|^2_{\mathcal{H}^{1/2}(\partial\Omega_1)},
$$

in which, for implementational reasons, all the norms are replaced by the $\ell^2-$norm.

(ii) The Dirichlet data (2.1b) and the current flux data (2.1d) come from practical measurements which are inherently contaminated with noisy errors, and we therefore replace $f$ and $g$ by $f^\varepsilon$ and $g^\varepsilon$, respectively, such that

$$
\|f^\varepsilon - f\|_{L^2(\partial\Omega_2)} \leq \varepsilon \quad \text{and} \quad \|g^\varepsilon - g\|_{L^2(\partial\Omega_2)} \leq \varepsilon. \quad (4.3)
$$

In computation, the noisy data are generated as

$$
f^\varepsilon(\boldsymbol{x}_j) = (1 + \rho_j \, p_f) \, f(\boldsymbol{x}_j), \quad g^\varepsilon(\boldsymbol{x}_j) = (1 + \rho_j \, p_g) \, g(\boldsymbol{x}_j), \quad j = \overline{N+1, N+M}, \quad (4.4)
$$

where $p_f$ and $p_g$ represent the percentage of noise added to the Dirichlet and Neumann boundary data on $\partial\Omega_2$, respectively, and $\rho_j$ is a pseudo-random noisy variable drawn from a uniform distribution in $[-1, 1]$ using the MATLAB command `-1+2*rand(1,M)`. In our numerical experiments it was observed that the effect of noise added to the Dirichlet boundary data was similar to that of perturbing the Neumann data. As a result in the numerical results section we only present results for noisy Neumann data, i.e. $p_g \neq 0$ and $p_f = 0$.

(iii) In (4.1), the outward normal vector $\boldsymbol{n}$ is defined as follows:

$$
\boldsymbol{n} = \begin{cases} \cos\vartheta \, \boldsymbol{i} + \sin\vartheta \, \boldsymbol{j}, & \text{if} \quad \boldsymbol{x} \in \partial\Omega_2, \\ \dfrac{1}{\sqrt{r^2(\vartheta) + r'^2(\vartheta)}} [-(r'(\vartheta)\sin\vartheta + r(\vartheta)\cos\vartheta) \, \boldsymbol{i} + (r'(\vartheta)\cos\vartheta - r(\vartheta)\sin\vartheta) \, \boldsymbol{j}], & \text{if} \quad \boldsymbol{x} \in \partial\Omega_1, \end{cases} \quad (4.5)
$$

where $\boldsymbol{i} = (1, 0)$ and $\boldsymbol{j} = (0, 1)$. As a result, from (3.1) the normal derivative $\partial_n u_N$ is evaluated as

$$
\partial_n u_N = \boldsymbol{n} \cdot \nabla u_N = -\frac{1}{2\pi} \sum_{k=1}^{2N} c_k \frac{(\boldsymbol{x} - \boldsymbol{\xi}_k) \cdot \boldsymbol{n}}{|\boldsymbol{x} - \boldsymbol{\xi}_k|^2}. \quad (4.6)
$$

In (4.5), we use the finite-difference approximation

$$r'(\vartheta_i) \approx \frac{r_{i+1} - r_{i-1}}{4\pi/N}, \quad i = \overline{1, N},\tag{4.7}$$

with the convention that $r_{N+1} = r_1$, $r_0 = r_N$.

(iv) Since the total number of unknowns is $3N + 4$ and the number of boundary condition collocation equations is $N + 2M$ we need to take $M \geq N + 2$.

(v) Since the inverse problem is ill-posed, in (4.1), the regularization terms $\lambda_1|\boldsymbol{c}|^2$ and $\lambda_2 \sum_{\ell=2}^{N} (r_\ell - r_{\ell-1})^2$ are added in order to achieve the stability of the numerical MFS solution $u_N$ and the smooth boundary $\partial\Omega_1$. We do not include regularization terms $\lambda_3|\boldsymbol{\eta}|^2$ and $\lambda_4|\boldsymbol{X}|^2$ since both $\boldsymbol{\eta}$ and $\boldsymbol{X}$ only have a small number of components (in this case two) and the numerical solution is expected to be stable in both $\boldsymbol{\eta}$ and $\boldsymbol{X}$.

4.1. **Non-linear minimization.** The minimization of functional (4.1) is carried out using the `MATLAB` [28] optimization toolbox routine `lsqnonlin` which solves nonlinear least squares problems. This is achieved using the `MATLAB` command

```
[x,resnorm,residual,exitflag,output] =
lsqnonlin(@f1,x0,lb,ub,
optimset('Display','iter','MaxFunEvals',mfe,'MaxIter',mi,'TolFun',tf,'TolX',tx))
```

The routine `lsqnonlin` by default uses the so-called trust-region-reflective algorithm based on the interior-reflective Newton method [3, 4].

The routine `lsqnonlin` terminates when

- the change in the solution vector $\boldsymbol{x}$ is less than the specified tolerance `tx`,
  or
- the change in the residual is less than the specified tolerance `tf`,
  or
- the number of iterations `mi` or the number of function evaluations `mfe` is exceeded.

The routine `lsqnonlin` does not require the user to provide the gradient and, in addition, it offers the option of imposing lower and upper bounds on the elements of the vector of unknowns $\boldsymbol{x} = [\boldsymbol{c}, \boldsymbol{r}, \boldsymbol{\eta}, \boldsymbol{C}]^T$ through the vectors `lb` and `up`. We can thus easily impose the constraints $0 < r_i < 1, \quad i = \overline{1, N}$, $0 < \eta_{int} < 1$, $1 < \eta_{ext} < S$ and $-R < X < R, -R < Y < R$. In our numerical experiments we chose $S = 4$. Moreover, we choose the initial vector of unknowns $\boldsymbol{x}_0 = (\boldsymbol{c}_0, \boldsymbol{r}_0, \eta_{int}, \eta_{ext}, X_0, Y_0)^T = (\boldsymbol{0}, \boldsymbol{0}.1, 0.5, 2, 0, 0)^T$.

## 5. Numerical examples

In the first three examples, the centre of the cavity $\boldsymbol{C} = [X, Y]^T$ is assumed to be known.

5.1. **Example 1.** We first consider an example for which the exact solution is known. Here we consider the case where $X = Y = 0$, $R = 1$ and $\alpha = 0$. In particular, we consider

$$\Omega_1 = \left\{ (x, y) \in \mathbb{R}^2 : x^2 + y^2 < R_0^2 < 1 \right\}, \qquad \Omega_2 = \left\{ (x, y) \in \mathbb{R}^2 : x^2 + y^2 < 1 \right\}\tag{5.1}$$

and

$$u(x, y) = \frac{x}{R_0^2} + \frac{x}{x^2 + y^2}.\tag{5.2}$$

For any $0 < R_0 < 1$, the function $u$ satisfies problem (2.1a)-(2.1d), with

$$f(x, y) = x \left( \frac{1}{R_0^2} + 1 \right) \quad \text{and} \quad g(x, y) = x \left( \frac{1}{R_0^2} - 1 \right), \quad (x, y) \in \partial\Omega_2.\tag{5.3}$$

Note that the compatibility condition (2.2) on the Neumann flux data $g$ is automatically satisfied.

In our numerical experiments we consider the case $R_0 = 0.5$.

In Figure 2 we present the reconstructed curves for various numbers of degrees of freedom obtained in 20 iterations, no noise and no regularization. From this figure it can be seen that very accurate and convergent numerical results are obtained. In Figures 3 and 4 we present typical examples of reconstructed curves with noise levels of $p_g = 5\%$ and 10%, respectively, with no regularization and $N = 48, M = 72$. From these figures it can be seen that if no regularization is employed then the numerical solution becomes unstable, provided that the number of iterations exceeds a certain threshold value which depends on the amount of noise $p_g$. On the other hand, the numerical solutions obtained after 20 to 50 iterations are very accurate and stable even if the input data are contaminated with quite a large amount of noise. In Figures 5 and 6 we present the corresponding reconstructed curves with noise levels of 5% and 10%, respectively, after 100 iterations and various regularization parameters $\lambda_1$ with $\lambda_2 = 0$. The corresponding curves for various regularization parameters $\lambda_2$ with $\lambda_1 = 0$ are presented in Figures 7 and 8. Overall, from Figures 2–8 it can be concluded that the numerical results are more accurate as the amount of noise decreases. Also, regularization with $\lambda_2$ (Figures 7 and 8) improves the stability of the numerical solution more than when regularization with $\lambda_1$ (Figures 5 and 6), or no regularization (Figures 3 and 4) is employed.
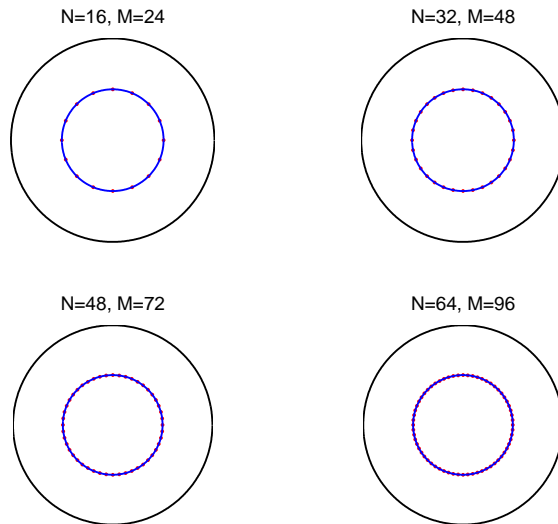


FIGURE 2. Example 1: Results for various numbers of degrees of freedom, no noise and no regularization.

5.2. **Example 2.** In this example, we consider a more complicated peanut-shaped cavity whose boundary $\partial\Omega_1$ is described by $X = Y = 0$, $R = 1$ and the radial parametrization

$$r(\vartheta) = \frac{3}{4}\sqrt{\cos^2(\vartheta) + 0.25\sin^2(\vartheta)}, \quad \vartheta \in [0, 2\pi), \tag{5.4}$$

in the case of $\alpha = 0$, which was considered in [12]. The Dirichlet data (2.1b) on $\partial\Omega_2$ is taken as [12]

$$u(1, \vartheta) = f(\vartheta) = \mathrm{e}^{-\cos^2 \vartheta}, \quad \vartheta \in [0, 2\pi). \tag{5.5}$$

Since in this case no analytical solution is available, the Neumann data (2.1d) is simulated by solving the direct mixed well-posed problem (2.1a), (2.1c) and (5.5), when $\partial\Omega_1$ is given by (5.4), using the MFS with $M = N = 200$. In order to avoid committing an inverse crime, the inverse solver is applied using $N = 48, M = 64$. Furthermore, noise is added as in (4.4).
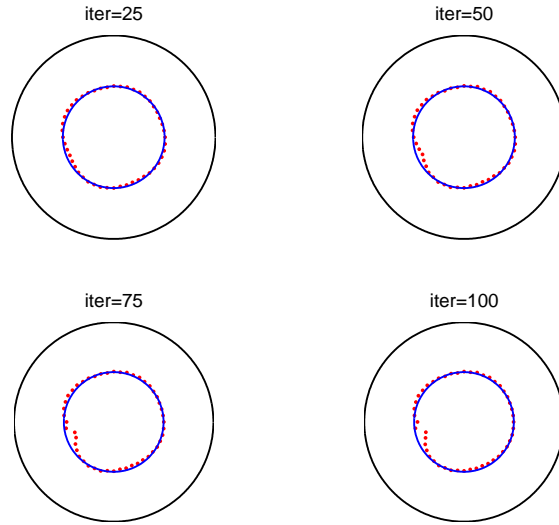
FIGURE 3. Example 1: Results for noise $p_g = 5\%$ and no regularization.
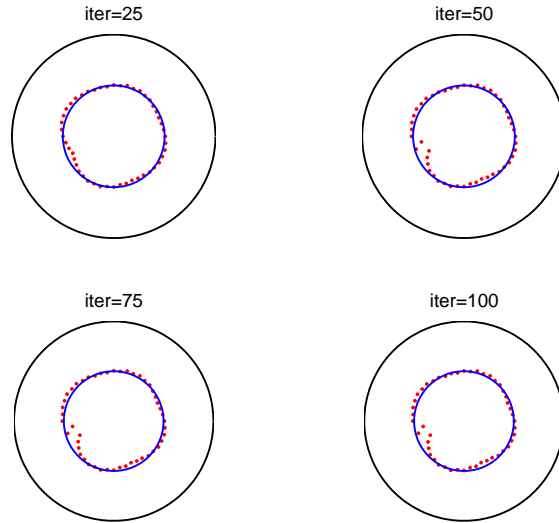


FIGURE 4. Example 1: Results for noise $p_g = 10\%$ and no regularization.

In Figures 9 and 10 we present the results obtained for different numbers of iterations, with noise $p_g = 0$ and 10%, respectively, and no regularization, i.e. $\lambda_1 = \lambda_2 = 0$. From these figures it can be seen that if no regularization is employed then the solution is quite accurate and remains the same between 100 and 1000 iterations. However, the unregularized numerical solution shown in Figure 10 for $p_g = 10\%$ will eventually become unstable if sufficiently
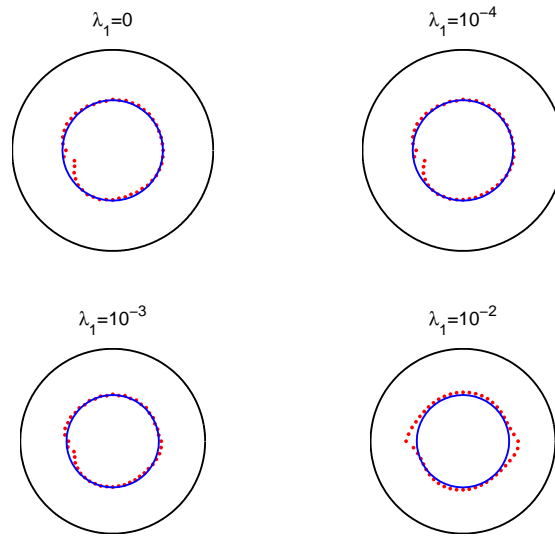
FIGURE 5. Example 1: Results for noise $p_g = 5\%$ and regularization with $\lambda_1$.
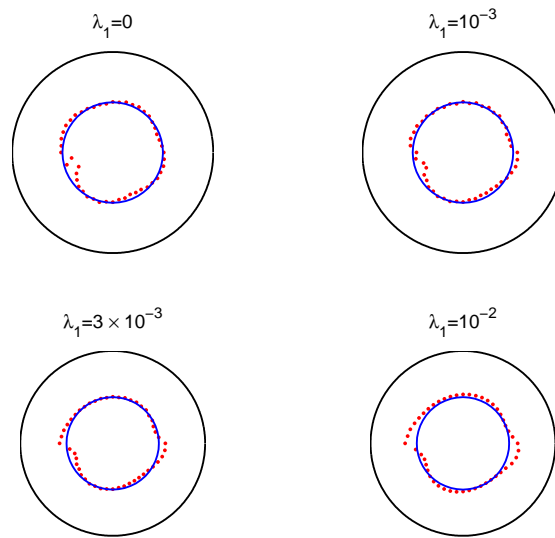


FIGURE 6. Example 1: Results for noise $p_g = 10\%$ and regularization with $\lambda_1$.

more iterations are considered. In Figures 11 and 12 we present the corresponding reconstructed curves with noise level of 10%, respectively, after 1000 iterations and various regularization parameters $\lambda_1$ when $\lambda_2 = 0$, and $\lambda_2$ when $\lambda_1 = 0$, respectively. From these figures it can be seen that the inclusion of regularization, either with $\lambda_1$ or $\lambda_2$, yields stable numerical solutions.

$\lambda_2=0$ $\lambda_2=0.1$

$\lambda_2=1$ $\lambda_2=10$
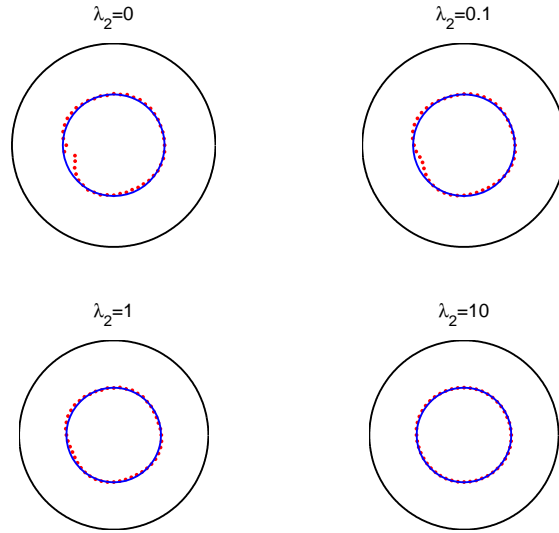
FIGURE 7. Example 1: Results for noise $p_g = 5\%$ and regularization with $\lambda_2$.

$\lambda_2=0$ $\lambda_2=0.1$

$\lambda_2=1$ $\lambda_2=10$
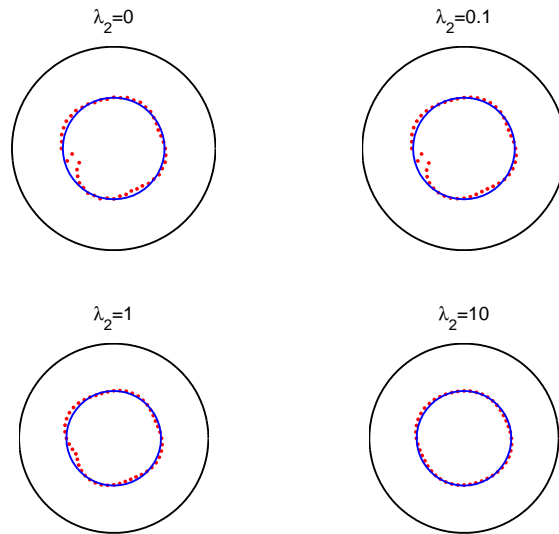
FIGURE 8. Example 1: Results for noise $p_g = 10\%$ and regularization with $\lambda_2$.

5.3. **Example 3.** We consider a bean-shaped cavity whose boundary $\partial\Omega_1$ is described by $X = Y = 0$, $R = 1$ and the radial parametrization

$$r(\vartheta) = \frac{0.5 + 0.4\cos(\vartheta) + 0.1\sin(2\vartheta)}{1 + 0.7\cos(\vartheta)}, \quad \vartheta \in [0, 2\pi), \tag{5.6}$$
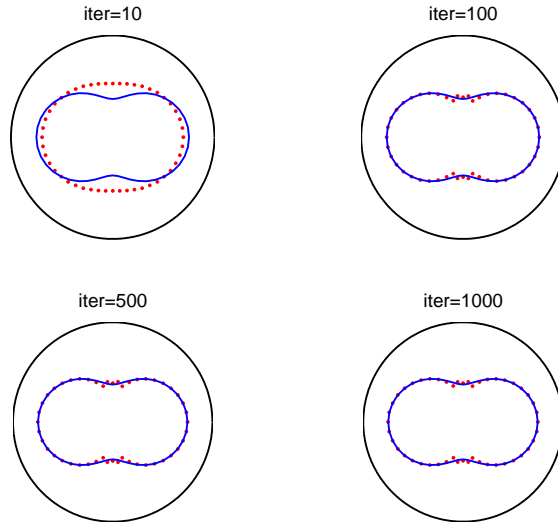
FIGURE 9. Example 2: Results for various numbers of iterations for no noise and no regularization.
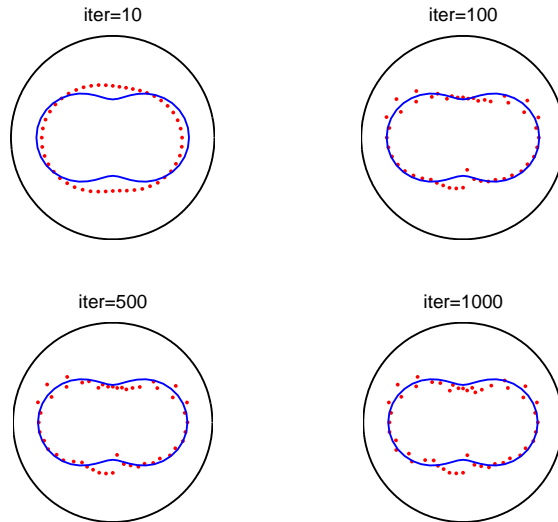


FIGURE 10. Example 2: Results for various numbers of iterations for noise $p_g = 10\%$ and no regularization.

in the case of $\alpha = 0$. This example, which was also considered in [12], is more difficult than Example 2 because of the presence of a sharp cusp-like portion mimicking a re-entrant corner. The Neumann data (2.1d) is simulated by solving the direct mixed well-posed problem (2.1a), (2.1c) and (5.5), when $\partial\Omega_1$ is given by (5.4), using the
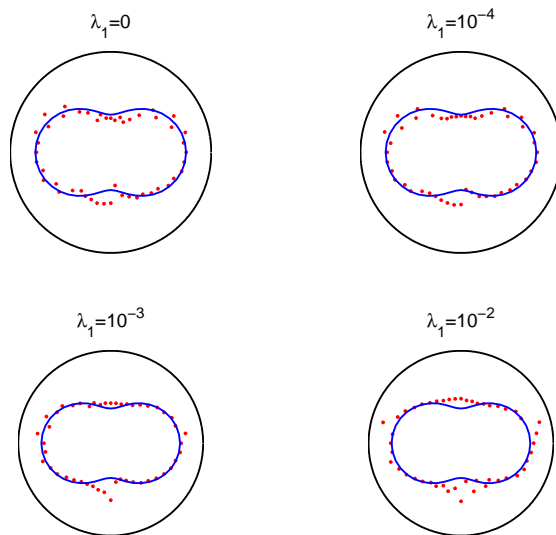
FIGURE 11. Example 2: Results for noise $p_g = 10\%$ and regularization with $\lambda_1$.
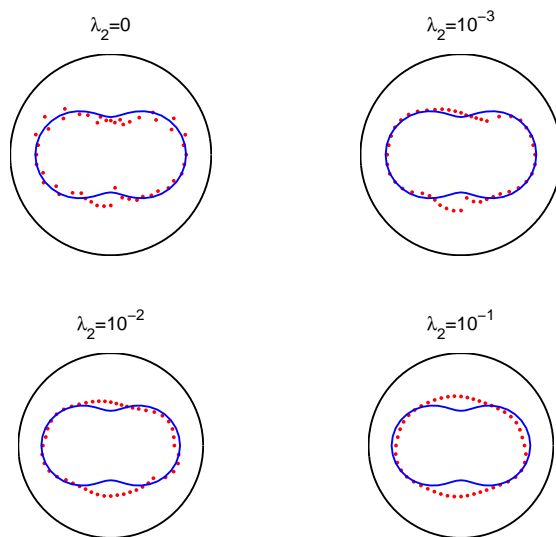
FIGURE 12. Example 2: Results for noise $p_g = 10\%$ and regularization with $\lambda_2$.

MFS with $M = N = 400$. In order to avoid committing an inverse crime, the inverse solver is applied using $N = 56, M = 64$. Noise is added to the data as in the previous examples.

In Figures 13 and 14 we present the results obtained for different numbers of iterations, no regularization, and $p = 0$ and $10\%$, respectively. In Figures 15 and 16 we present the corresponding reconstructed curves for the noise

level of $p_g = 10\%$, after 1000 iterations and various regularization parameters $\lambda_1$ with $\lambda_2 = 0$, and $\lambda_2$ with $\lambda_1 = 0$, respectively. The same conclusions as in the previous example are obtained, compare Figures 9–12 of Example 2 with Figures 13–16 of Example 3.
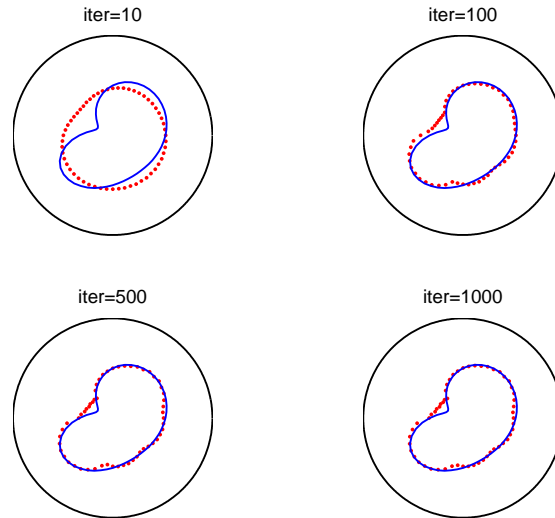


FIGURE 13. Example 3: Results for various numbers of iterations, no noise and no regularization.
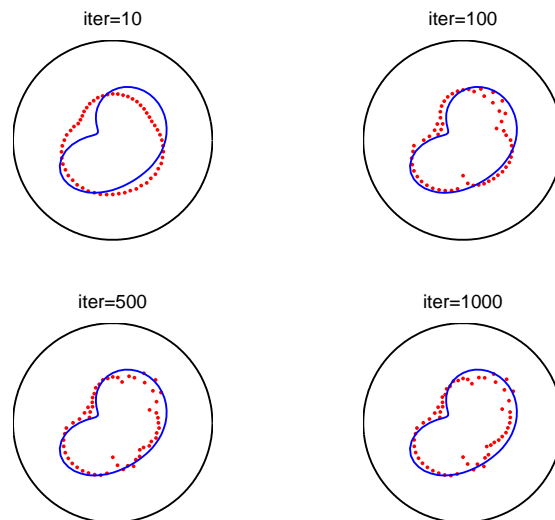


FIGURE 14. Example 3: Results for various numbers of iterations for noise $p_g = 10\%$ and no regularization.
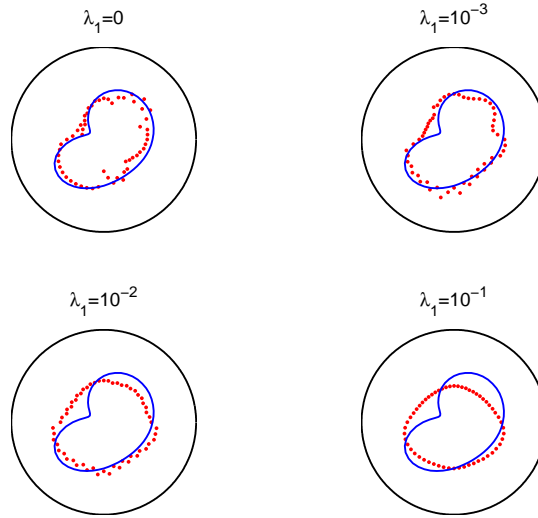
FIGURE 15. Example 3: Results for noise $p_g = 10\%$ and regularization with $\lambda_1$.
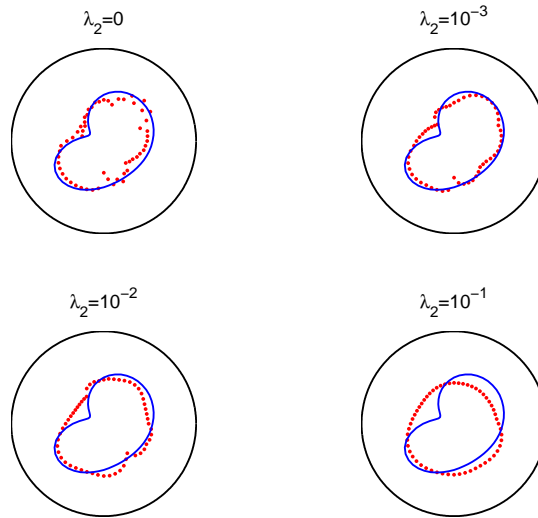


FIGURE 16. Example 3: Results for noise $p_g = 10\%$ and regularization with $\lambda_2$.

5.4. **Example 4.** We consider an obstacle $\Omega_1$ described by $X = 0.5, Y = -1, R = 3.5$ and the radial parametrization

$$r(\vartheta) = 1.52 - 0.24\sin(3\vartheta), \quad \vartheta \in [0, 2\pi), \tag{5.7}$$

in the case of $\alpha = 0$. This example, which was considered in [26] for the Stokes equations in slow viscous flow, is more difficult than the previous examples because of the fact that the coordinates of the centre of the cavity are unknown. The Neumann data (2.1d) is simulated by solving the direct mixed well-posed problem (2.1a), (2.1c) and (5.5), when $\partial\Omega_1$ is given by (5.7), using the MFS with $M = N = 400$. In order to avoid committing an inverse crime, the inverse solver is applied using $N = 56, M = 64$.

In Figures 17 and 18 we present the results obtained for different numbers of iterations, no regularization, and $p_g = 0$ and $3\%$, respectively. In Figures 19 and 20 we present the corresponding reconstructed curves with a noise level of $p_g = 3\%$ after 1000 iterations and various levels of regularization $\lambda_1$ with $\lambda_2 = 0$, and $\lambda_2$ with $\lambda_1 = 0$, respectively. The L-curves [10, 9] obtained with regularization in $\lambda_1$ and $\lambda_2$ for noise $p_g = 3\%$ and 1000 iterations are presented in Figures 21(a) and (b), respectively. These indicate that the corresponding optimal values of the regularization parameters are $\lambda_1 = 10^{-4}$ and $\lambda_2 = 0$, and $\lambda_1 = 0$ and $\lambda_2 = 10^{-4}$, as confirmed from Figures 19 and 20, respectively. Also, from Figures 19 and 20 it can be seen that regularization with $\lambda_2$ is more accurate and stable than with $\lambda_1$.
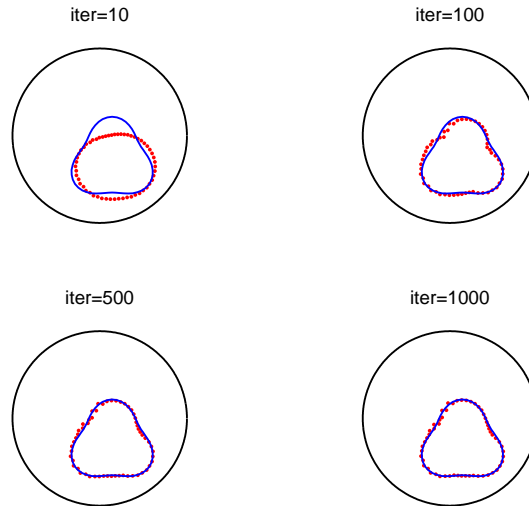


FIGURE 17. Example 4: Results for various numbers of iterations for no noise and no regularization.

5.5. **Example 5.** We finally consider the case when obstacle $\Omega_1$ is a square of side 2, rotated by $\pi/4$, described by $X = -0.5, Y = 1.2, R = 3.5$, in the case of $\alpha = 1$. This has the following radial parametrization

$$r(\vartheta) = \begin{cases} \dfrac{\sqrt{2}}{\cos(\vartheta) + \sin(\vartheta)} & \vartheta \in [0, \dfrac{\pi}{2}), \\ \dfrac{\sqrt{2}}{-\cos(\vartheta) + \sin(\vartheta)} & \vartheta \in [\dfrac{\pi}{2}, \pi), \\ -\dfrac{\sqrt{2}}{\cos(\vartheta) + \sin(\vartheta)} & \vartheta \in [\pi, \dfrac{3\pi}{2}), \\ \dfrac{\sqrt{2}}{\cos(\vartheta) - \sin(\vartheta)} & \vartheta \in [\dfrac{3\pi}{2}, 2\pi). \end{cases} \tag{5.8}$$
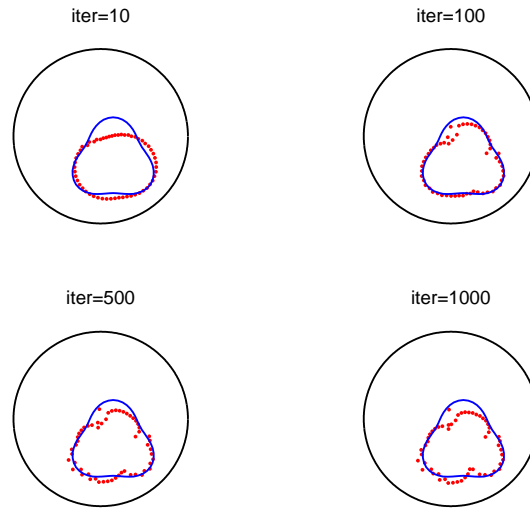
FIGURE 18. Example 4: Results for various numbers of iterations for noise $p_g = 3\%$ and no regularization.
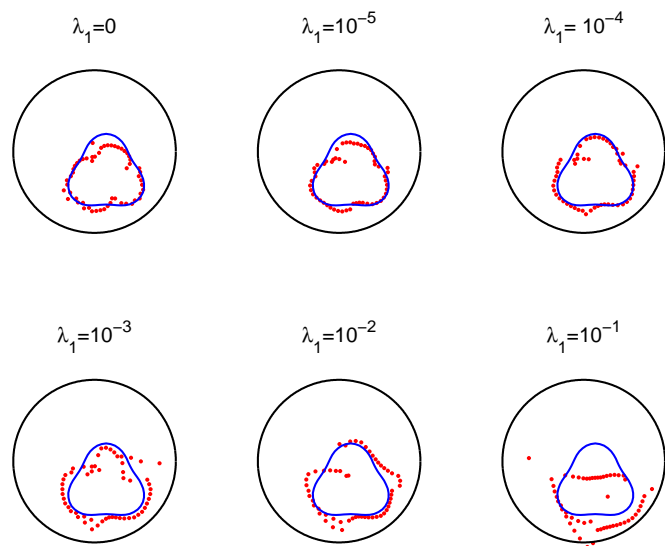


FIGURE 19. Example 4: Results for noise $p_g = 3\%$ and regularization with $\lambda_1$.

This example which is similar to the one considered in [25], but for a boundary determination problem, is more difficult than the previous examples because the coordinates of the centre of the rigid inclusion are unknown and
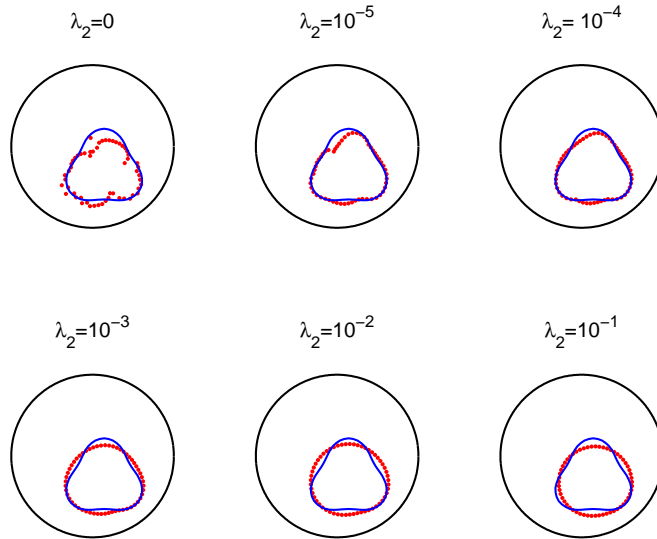
FIGURE 20. Example 4: Results for noise $p_g = 3\%$ and regularization with $\lambda_2$.
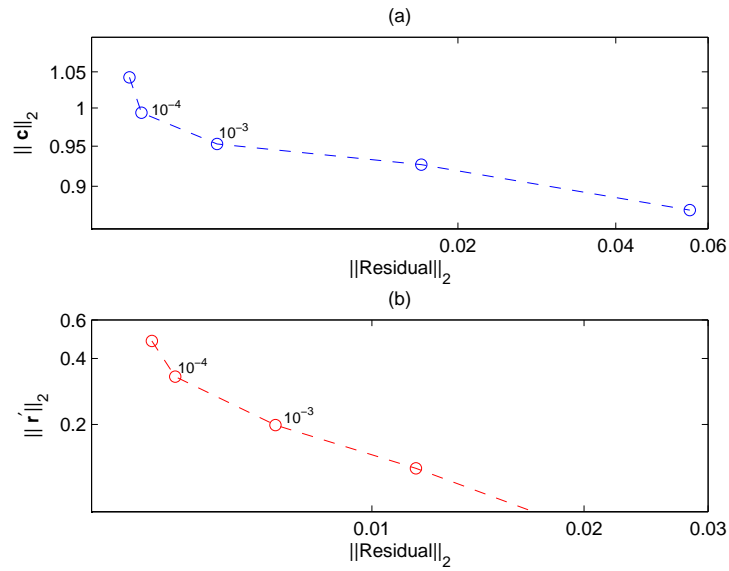


FIGURE 21. Example 4: L-curves obtained with regularization in (a) $\lambda_1$ and (b) $\lambda_2$ for noise $p_g = 3\%$.

also its boundary is now piecewise smooth. The Neumann data (2.1d) is numerically simulated by solving the

direct Dirichlet well-posed problem (2.1a), (2.1c) and (5.5), when $\partial\Omega_1$ is given by (5.8), using the MFS with $M = N = 400$. In order to avoid committing an inverse crime, the inverse solver is applied using $N = 56, M = 64$.

In Figures 22 and 23 we present the results obtained for different numbers of iterations, no regularization, and $p_g = 0$ and 5%, respectively. In Figures 24 and 25 we present the corresponding reconstructed curves obtained with a noise level of $p_g = 5\%$, 100 iterations and various levels of regularization $\lambda_1$ with $\lambda_2 = 0$, and $\lambda_2$ with $\lambda_1 = 0$, respectively. From Figure 22 it can be seen that in the case of no noise the numerical solution is accurate and almost unchanged for iteration numbers between 10 and 100. However, for 5% noise the solution becomes visibly unstable as the number of iterations increases beyond 50 when no regularization is employed, see Figure 23. However, the unstable numerical solution shown in Figure 23 for 100 iterations can be further stabilized by employing regularization with either $\lambda_1$, see Figure 24 for $\lambda_1 = 10^{-4}$ to $10^{-2}$, or $\lambda_2$, see Figure 25 for $\lambda_2 = 10^{-4}$ to $10^{-1}$.
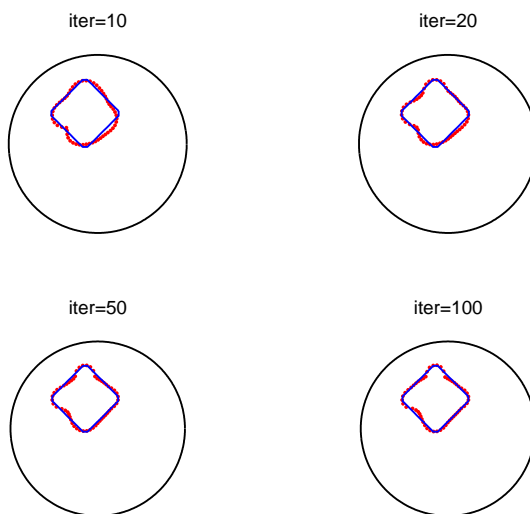


FIGURE 22. Example 5: Results for various numbers of iterations for no noise and no regularization.

## 6. EXTENSION TO MULTIPLE VOIDS

The MFS analysis performed so far showed the successful implementation of this method for the identification of a single void. In this section we extend the analysis to multiple voids which may contain both cavities and rigid inclusions. For the sake of clarity, we describe the formulation for the case of two cavities. Therefore, we consider the inverse problem

$$\Delta u = 0 \quad \text{in} \quad \Omega, \tag{6.1a}$$

subject to the boundary conditions

$$u = f \quad \text{and} \quad \partial_n u = g \quad \text{on} \quad \partial\Omega_2, \tag{6.1b}$$

and the homogeneous boundary conditions

$$\alpha_1 u + (1 - \alpha_1)\partial_n u = 0 \quad \text{on} \quad \partial\Omega_1^a, \quad \text{where} \quad \alpha_1 \in \{0, 1\}, \tag{6.1c}$$
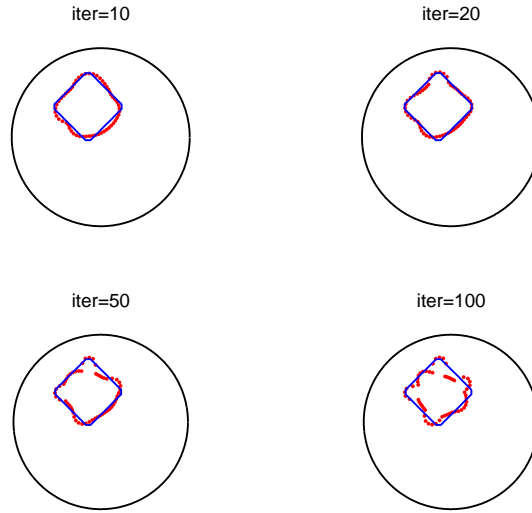
FIGURE 23. Example 5: Results for various numbers of iterations for noise $p_g = 5\%$ and no regularization.
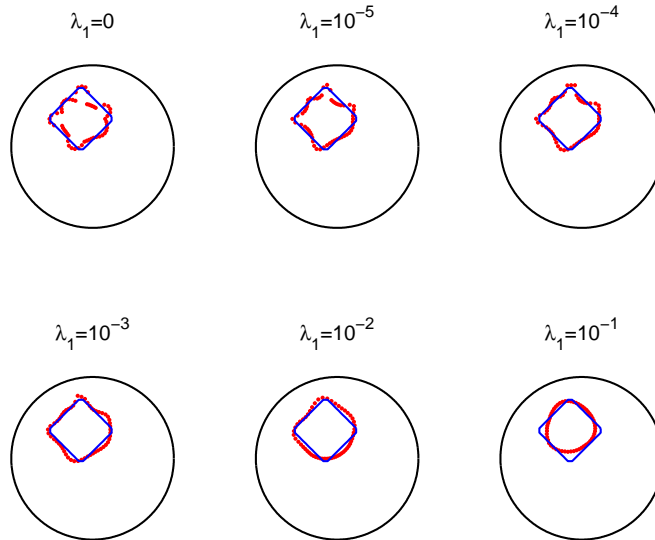


FIGURE 24. Example 5: Results for noise $p_g = 5\%$ and regularization with $\lambda_1$.

and

$$\alpha_2 u + (1 - \alpha_2)\partial_n u = 0 \quad \text{on} \quad \partial\Omega_1^b, \quad \text{where} \quad \alpha_2 \in \{0, 1\}. \tag{6.1d}$$
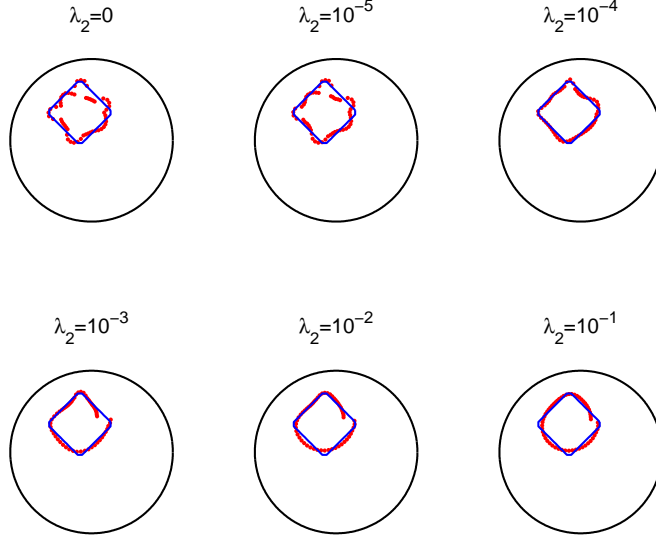
FIGURE 25. Example 5: Results for noise $p_g = 5\%$ and regularization with $\lambda_2$.

Here $\Omega_1^a$ and $\Omega_1^b$ are two disjoint voids, such that $\Omega_1^a \cup \Omega_1^b = \Omega_1$ and $\overline{\Omega_1^a} \cap \overline{\Omega_1^b} = \emptyset$.
We seek an approximation of the form

$$u_N(\boldsymbol{c}, \boldsymbol{\xi}; \boldsymbol{x}) = \sum_{k=1}^{3N} c_k \, G(\boldsymbol{\xi}_k, \boldsymbol{x}), \quad \boldsymbol{x} \in \overline{\Omega}. \tag{6.2}$$

The sources $(\boldsymbol{\xi}_k)_{k=\overline{1,3N}}$ are located outside the solution domain $\Omega$, i.e. in $\Omega_1 \cup \left(\mathbb{R}^2 \backslash \overline{\Omega}_2\right)$. In particular, $(\boldsymbol{\xi}_k)_{k=\overline{1,N}} \in \Omega_1^a$ are placed on a (moving) pseudo-boundary $\partial\Omega_1^{a\prime}$ similar (contraction) to $\partial\Omega_1^a$, $(\boldsymbol{\xi}_k)_{k=\overline{N+1,2N}} \in \Omega_1^b$ are placed on a (moving) pseudo-boundary $\partial\Omega_1^{b\prime}$ similar (contraction) to $\partial\Omega_1^b$, while $(\boldsymbol{\xi}_k)_{k=\overline{2N+1,3N}} \in \mathbb{R}^2 \backslash \overline{\Omega}_2$ are also placed on a (moving) pseudo-boundary $\partial\Omega_2'$ similar (dilation) to $\partial\Omega_2$. The situation is depicted in Figure 26. The contraction parameters for $\partial\Omega_1^{a\prime}$ and $\partial\Omega_1^{b\prime}$ are taken to be $\eta_{int}^a \in (0,1)$ and $\eta_{int}^b \in (0,1)$, respectively.
The outer boundary collocation and source points are chosen as

$$\boldsymbol{x}_{2N+\ell} = R(\cos\tilde{\vartheta}_\ell, \sin\tilde{\vartheta}_\ell), \quad \ell = \overline{1,M}, \tag{6.3}$$

$$\boldsymbol{\xi}_{2N+k} = \eta_{ext} R(\cos\vartheta_k, \sin\vartheta_k), \quad k = \overline{1,N}, \tag{6.4}$$

respectively, where $\tilde{\vartheta}_\ell = \frac{2\pi(\ell-1)}{M}$, $\ell = \overline{1,M}$ and $\vartheta_k = \frac{2\pi(k-1)}{N}$, $k = \overline{1,N}$, and the (unknown) parameter $\eta_{ext} \in (1,S)$ with $S > 1$ prescribed.
We further assume that the unknown boundaries $\partial\Omega_1^a$ and $\partial\Omega_1^b$ are a smooth, star-like curves with respect to their centres which have unknown coordinates $(X^a, Y^a)$ and $(X^b, Y^b)$, respectively. This means that their equations in polar coordinates can be written as

$$x = X^a + r^a(\vartheta)\cos\vartheta, \qquad y = Y^a + r^a(\vartheta)\sin\vartheta, \tag{6.5}$$

$$x = X^b + r^b(\vartheta)\cos\vartheta, \qquad y = Y^b + r^b(\vartheta)\sin\vartheta, \qquad \vartheta \in [0, 2\pi), \tag{6.6}$$

where $r^a$ and $r^b$ are smooth $2\pi-$periodic functions.
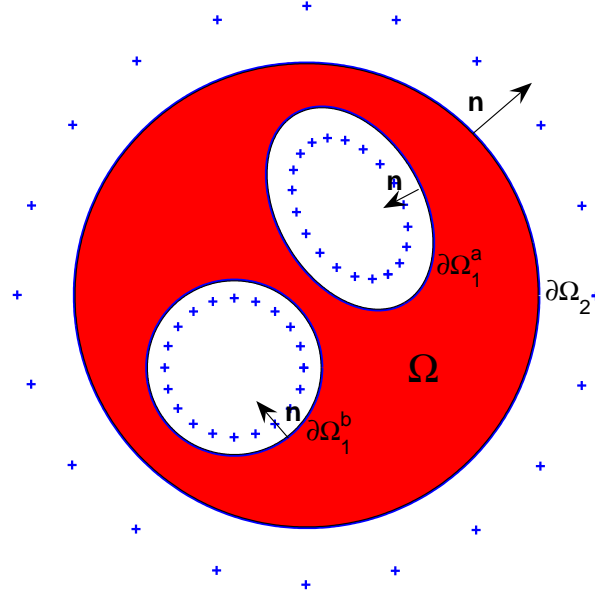
FIGURE 26. Geometry of the problem with two inclusions. The crosses (+) denote the source points.

The discretized forms of (6.5) and (6.6) for $\partial\Omega_1^a$ and $\partial\Omega_1^b$ become

$$r_k^a = r^a(\vartheta_k), \quad r_k^b = r^b(\vartheta_k) \qquad k = \overline{1, N}. \tag{6.7}$$

We choose the inner boundary collocation and source points as

$$
\begin{aligned}
\boldsymbol{x}_k &= (X^a, Y^a) + r_k^a \left(\cos\vartheta_k, \sin\vartheta_k\right), & k &= \overline{1, N} & (6.8)\\
\boldsymbol{x}_k &= (X^b, Y^a) + r_k^b \left(\cos\vartheta_k, \sin\vartheta_k\right), & k &= \overline{N+1, 2N} & (6.9)\\
\boldsymbol{\xi}_k &= (X^a, Y^a) + \eta_{int}^a\, r_k^a \left(\cos\vartheta_k, \sin\vartheta_k\right), & k &= \overline{1, N}, & (6.10)\\
\boldsymbol{\xi}_k &= (X^b, Y^b) + \eta_{int}^b\, r_k^b \left(\cos\vartheta_k, \sin\vartheta_k\right), & k &= \overline{N+1, 2N}. & (6.11)
\end{aligned}
$$

The coefficients $(c_k)_{k=\overline{1,3N}}$ in (6.2), the radii $(r_k^a)_{k=\overline{1,N}}, (r_k^b)_{k=\overline{1,N}} \in (0,1)$ in (6.7), the contraction and dilation coefficients $\eta_{int}^a, \eta_{int}^b$ and $\eta_{ext}$, and the coordinates of the centres $(X^a, Y^a), (X^b, Y^b)$ can be determined by imposing

the boundary conditions in a least-squares sense. This leads to the minimization of the functional

$$
\begin{aligned}
S(\boldsymbol{c}, \boldsymbol{r}^a, \boldsymbol{r}^b, \boldsymbol{\eta}, \boldsymbol{C}) : \quad = \quad & \sum_{j=2N+1}^{2N+M} [u_N(\boldsymbol{c}, \boldsymbol{\xi}; \boldsymbol{x}_j) - f^\varepsilon(\boldsymbol{x}_j)]^2 + \sum_{j=2N+1}^{2N+M} [\partial_n u_N(\boldsymbol{c}, \boldsymbol{\xi}; \boldsymbol{x}_j) - g^\varepsilon(\boldsymbol{x}_j)]^2 \\
& + \sum_{j=1}^{N} [\alpha_1 u_N(\boldsymbol{c}, \boldsymbol{\xi}; \boldsymbol{x}_j) + (1-\alpha_1)\partial_n u_N(\boldsymbol{c}, \boldsymbol{\xi}; \boldsymbol{x}_j)]^2 \\
& + \sum_{j=N+1}^{2N} [\alpha_2 u_N(\boldsymbol{c}, \boldsymbol{\xi}; \boldsymbol{x}_j) + (1-\alpha_2)\partial_n u_N(\boldsymbol{c}, \boldsymbol{\xi}; \boldsymbol{x}_j)]^2 \\
& + \lambda_1 |\boldsymbol{c}|^2 + \lambda_2^a \sum_{\ell=2}^{N} (r_\ell^a - r_{\ell-1}^a)^2 + \lambda_2^b \sum_{\ell=2}^{N} (r_\ell^b - r_{\ell-1}^b)^2,
\end{aligned}
\tag{6.12}
$$

where $\lambda_1, \lambda_2^a, \lambda_2^b \geq 0$ are regularization parameters to be prescribed, $\boldsymbol{c} = [c_1, c_2, \ldots, c_{3N}]^T, \boldsymbol{r}^a = [r_1^a, r_2^a, \ldots, r_N^a]^T,$
$\boldsymbol{r}^b = [r_1^b, r_2^b, \ldots, r_N^b]^T, \boldsymbol{\eta} = [\eta_{int}^a, \eta_{int}^b, \eta_{ext}]^T$ and $\boldsymbol{C} = [X^a, Y^a, X^b, Y^b]^T.$
The number of unknowns is $5N+7$ and the number of boundary collocation equations $2N+2M$, and thus we need to take $2M \geq 3N+7$.
In the case of multiple voids, the assumption that the voids stay disjoint requires some manual adjustments in the iteration process in order to avoid the intersection of the approximating curves $\partial\Omega_1^a$ and $\partial\Omega_1^b$.

6.1. **Example 6.** We consider the case when two obstacles $\Omega_1^a$ and $\Omega_1^b$ are present. $\Omega_1^a$ is a disk of radius 1, with centre $X^a = 1, Y^a = -1$, while $\Omega_1^b$ is described by the radial parametrization

$$
r(\vartheta) = \frac{1 + 0.8\cos(\vartheta) + 0.2\sin(2\vartheta)}{1 + 0.7\cos(\vartheta)}, \quad \vartheta \in [0, 2\pi),
\tag{6.13}
$$

and has centre $X^b = -1, Y^b = 1$. In this example $R = 3.5$ and we consider Dirichlet boundary conditions $(\alpha_1 = \alpha_2 = 1)$ on the boundaries of both rigid inclusions. The Neumann data (2.1d) is simulated by solving the direct problem using the MFS with $M = N = 400$. In order to avoid committing an inverse crime, the inverse solver is applied using $N = 40, M = 64$.

In Figures 27 and 28 we present the results obtained for different numbers of iterations, no regularization, and $p_g = 0$ and 5%, respectively. In Figures 29 and 30 we present the corresponding reconstructed curves with a noise level of $p_g = 5\%$, after 100 iterations, and various levels of regularization $\lambda_1$ with $\lambda_2 = \lambda_2^a = \lambda_2^b = 0$, and $\lambda_1 = 0$ with $\lambda_2 = \lambda_2^a = \lambda_2^b$, respectively. Overall, Figures 27–30 illustrate that the MFS can indeed retrieve successfully voids having two connected components.

## 7. Conclusions

In this paper we propose a new MFS algorithm for the solution of inverse geometric problems. This algorithm has the following features:

- It is based on the so-called *dynamic* approach in which the location of the pseudo-boundaries is taken to be unknown and has to be determined as part of the solution. This algorithm to a large extent resolves, in a natural way, one of the major issues related to the MFS, namely the problem of the initial placement of the sources. This is so because of the non-linear nature of the type of problems investigated. In previous investigations the exterior pseudo-boundary was pre-assigned while the interior boundary was selected based on an *a posteriori* approach similar to the one used in [31].
- In addition, in contrast to previous applications of the MFS to such inverse problems, we consider problems in which the centre of the void to be reconstructed is unknown. The coordinates of the centre are merely taken as additional unknowns in the algorithm.
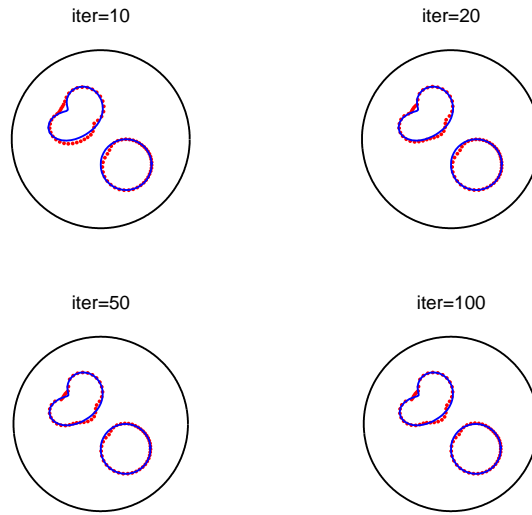
FIGURE 27. Example 6: Results for various numbers of iterations for no noise and no regularization.
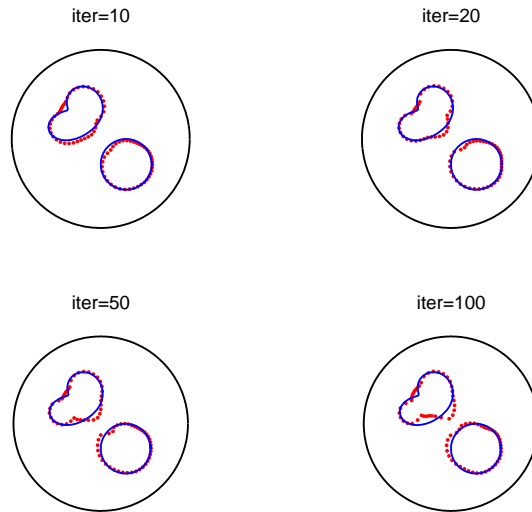


FIGURE 28. Example 6: Results for various numbers of iterations for noise $p_g = 5\%$ and no regularization.

- The `MATLAB` optimization toolbox routine `lsqnonlin` is used, for the first time, instead of the MINPACK [6] routine `lmdif`. While both routines are designed to solve nonlinear least squares problems, the former allows for the imposition of simple bounds on the variables. This facilitates, from the start, the elimination of physically unrealistic solutions.
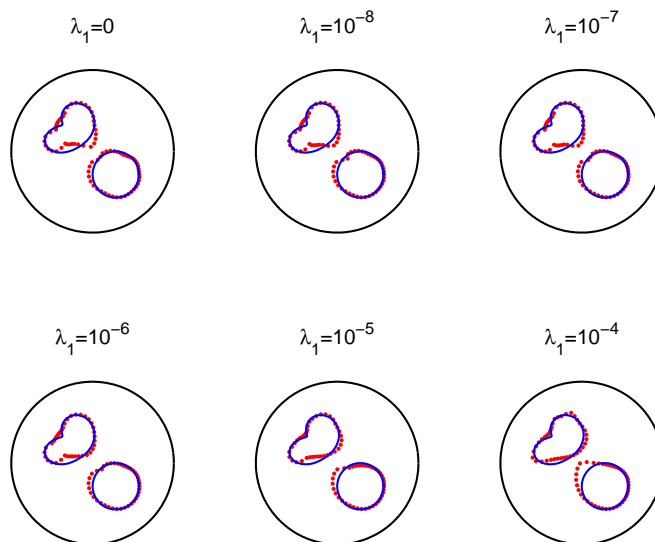
FIGURE 29. Example 6: Results for noise $p_g = 5\%$ and regularization with $\lambda_1$.

- The stability of the proposed algorithm is achieved using two regularization parameters while their optimal values can be determined by the use of the L-curve criterion. The method is shown to accurately reconstruct smooth or piecewise smooth, convex or concave, single or multiple cavities and rigid inclusions.

Future applications of the proposed algorithm will include inverse geometric problems governed by different linear partial differential equations in two dimensions, such as the Laplace-Beltrami equation, Helmholtz-type equations and the Lamé system, and extensions to three-dimensions.

## References

[1] M. A. Aleksidze, *On the question of a practical application of a new approximation method*, Differencial'nye Uravnenija **2** (1966), 1625–1629.

[2] G. Alessandrini and L. Rondi, *Optimal stability for the inverse problem of multiple cavities*, J. Diff. Equations **176** (2001), 356–386.

[3] T. F. Coleman and Y. Li, *On the convergence of interior-reflective Newton methods for nonlinear minimization subject to bounds*, Math. Programming **67** (1994), 189–224.

[4] _____, *An interior trust region approach for nonlinear minimization subject to bounds*, SIAM J. Optim. **6** (1996), 418–445.

[5] G. Fairweather and R. L. Johnston, *The method of fundamental solutions for problems in potential theory*, Treatment of Integral Equations by Numerical Methods, Academic Press, London, 1982, pp. 349–359.

[6] B. S. Garbow, Hillstrom. K. E., and J. J. Moré, *Minpack project*, Argonne National Laboratory, 1980.

[7] P. Gorzelańczyk and J. A. Kołodziej, *Some remarks concerning the shape of the source contour with application of the method of fundamental solutions to elastic torsion of prismatic rods*, Eng. Anal. Bound. Elem. **37** (2008), 64–75.
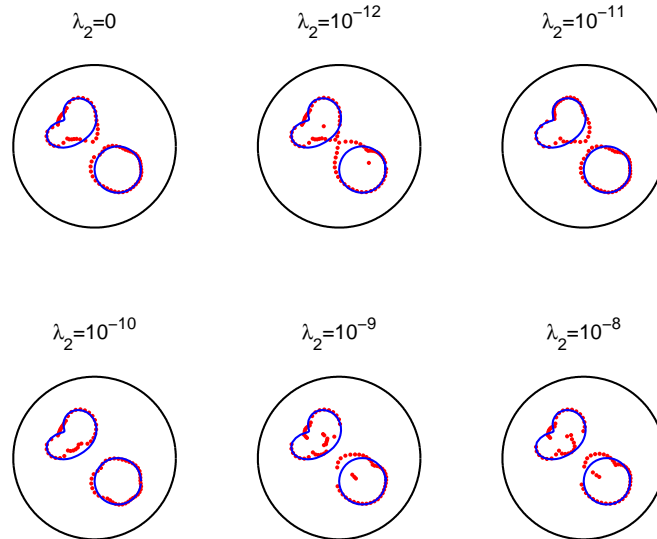
FIGURE 30. Example 6: Results for noise $p_g = 5\%$ and regularization with $\lambda_2$.

[8] H. Haddar and R. Kress, *Conformal mappings and inverse boundary value problems*, Inverse Problems **21** (2005), 935–953.

[9] P. C. Hansen, *Discrete Inverse Problems: Insight and Algorithms*, SIAM, Philadelphia, 2010.

[10] P. C. Hansen and D. P. O'Leary, *The use of the L-curve in the regularization of discrete ill-posed problems*, SIAM J. Sci. Comput. **14** (1993), 1487–1503.

[11] S. Ho-Tai, R. S. Johnston, and R. Mathon, *Software for Solving Boundary Value Problems for Laplace's Equation using Fundamental Solutions*, Tech. Report Technical Report 136/79, Department of Computer Science, University of Toronto, 1979.

[12] O. Ivanyshyn and R. Kress, *Nonlinear integral equations for solving inverse boundary value problems for inclusions and cracks*, J. Integral Equations Appl. **18** (2006), no. 1, 13–38.

[13] R. L. Johnston and G. Fairweather, *The method of fundamental solutions for problems in potential flow*, Appl. Math. Model. **8** (1984), 265–270.

[14] R. L. Johnston and R. Mathon, *The computation of electric dipole fields in conducting media*, Internat. J. Numer. Methods Engrg. **14** (1979), 1739–1760.

[15] A. Karageorghis and G. Fairweather, *The method of fundamental solutions for the numerical solution of the biharmonic equation*, J. Comput. Phys. **69** (1987), 434–459.

[16] A. Karageorghis and G. Fairweather, *The method of fundamental solutions for the solution of nonlinear plane potential problems*, IMA J. Numer. Anal. **9** (1989), 231–242.

[17] A. Karageorghis and G. Fairweather, *The method of fundamental solutions for axisymmetric potential problems*, Int. J. Numer. Meth. Engng. **44** (1999), 1653–1669.

[18] A. Karageorghis and D. Lesnic, *The method of fundamental solutions for steady-state heat conduction in nonlinear materials*, Commun. Comput. Phys. **4** (2008), 911–928.

[19] _____, *Steady-state nonlinear heat conduction in composite materials using the method of fundamental solutions*, Comput. Methods Appl. Mech. Engrg. **197** (2008), 3122–3137.

[20] _____, *Detection of cavities using the method of fundamental solutions*, Inverse Probl. Sci. Eng. **17** (2009), 803–820.

[21] A. Karageorghis, D. Lesnic, and L. Marin, *A survey of applications of the MFS to inverse problems*, Inverse Probl. Sci. Eng. **19** (2011), 309–336.

[22] V. D. Kupradze, *On a method of solving approximately the limiting problems of mathematical physics*, Comput. Math. Math. Phys. **4** (1964), 199–205.

[23] _____, *Potential Methods in the Theory of Elasticity*, Israel Program for Scientific Translations, Jerusalem, 1965.

[24] V. D. Kupradze and M. A. Aleksidze, *The method of functional equations for the approximate solution of certain boundary value problems*, Comput. Math. Math. Phys. **4** (1964), 82–126.

[25] L. Marin, A. Karageorghis, and D. Lesnic, *The MFS for numerical boundary identification in two-dimensional harmonic problems*, Eng. Anal. Bound. Elem. **35** (2011), 342–354.

[26] N. F. M. Martins and A. L. Silvestre, *An iterative MFS approach for the detection of immersed obstacles*, Eng. Anal. Bound. Elem. **32** (2008), 517–524.

[27] R. Mathon and R. L. Johnston, *The approximate solution of elliptic boundary–value problems by fundamental solutions*, SIAM J. Numer. Anal. **14** (1977), 638–650.

[28] The MathWorks, Inc., 3 Apple Hill Dr., Natick, MA, *Matlab*.

[29] A. Poullikkas, A. Karageorghis, G. Georgiou, and J. Ascough, *The method of fundamental solutions for Stokes flows with a free surface*, Numer. Methods Partial Differential Equations **14** (1998), 667–678.

[30] L. Rondi, *Uniqueness and Optimal Stability for the Determination of Multiple Defects by Electrostatic Measurements*, Ph.D. thesis, University of Trieste, 1999, `http://www.sissa.it/library/Thesis/rondi99.ps`.

[31] R. Tankelevich, G. Fairweather, A. Karageorghis, and Y.-S. Smyrlis, *Potential field based geometric modelling using the method of fundamental solutions*, Internat. J. Numer. Methods Engrg. **68** (2006), 1257–1280.

Department of Mathematics and Statistics, University of Cyprus/ Πανεπιστημιο Κυπρου, P.O.Box 20537, 1678 Nicosia/Λευκωσια, Cyprus/Κυπρος
*E-mail address*: `andreask@ucy.ac.cy`

Department of Applied Mathematics, University of Leeds, Leeds LS2 9JT, UK
*E-mail address*: `amt5ld@maths.leeds.ac.uk`

Institute of Solid Mechanics, Romanian Academy, 15 Constantin Mille, 010141 Bucharest, and Centre for Continuum Mechanics, Faculty of Mathematics and Computer Science, University of Bucharest, 14 Academiei, 010014 Bucharest, Romania
*E-mail address*: `marin.liviu@gmail.com; liviu@imsar.bu.edu.ro`